Article

pubs.acs.org/Biomac

Multimeric Disintegrin Protein Polymer Fusions That Target Tumor Vasculature

Siti M. Janib,[†,‡,§] Joshua A. Gustafson,[†,‡] Radu O. Minea,[∥] Stephen D. Swenson,[∥] Shuanglong Liu,[⊥] Martha K. Pastuszka,[‡] Lye Lin Lock,[#] Honggang Cui,[#] Francis S. Markland,[∥] Peter S. Conti,[‡,⊥,○] Zibo Li,[⊥] and J. Andrew MacKay*[,‡,○]

[‡]Department of Pharmacology and Pharmaceutical Sciences, School of Pharmacy, [§]Medical Technology Division, Malaysian Nuclear Agency, Bangi, 43000 Kajang Selangor, Malaysia

[∥]Department of Biochemistry and Molecular Biology, Norris Comprehensive Cancer Center, Keck School of Medicine, and [⊥]Department of Radiology, Keck School of Medicine, Molecular Imaging Center, University of Southern California, Los Angeles, California 90033, United States

[#]Department of Chemical and Biomolecular Engineering, Johns Hopkins University, Baltimore, Maryland 21218, United States

[○]Department of Biomedical Engineering, Viterbi School of Engineering, University of Southern California, Los Angeles California 90089, United States

Supporting Information

ABSTRACT: Recombinant protein therapeutics have increased in number and frequency since the introduction of human insulin, 25 years ago. Presently, proteins and peptides are commonly used in the clinic. However, the incorporation of peptides into clinically approved nanomedicines has been limited. Reasons for this include the challenges of decorating pharmaceutical-grade nanoparticles with proteins by a process that is robust, scalable, and cost-effective. As an alternative to covalent bioconjugation between a protein and nanoparticle, we report that biologically active proteins may themselves mediate the formation of small multimers through steric stabilization by large protein polymers. Unlike multistep purification and bioconjugation, this approach is completed during biosynthesis. As proof-of-principle, the disintegrin protein called vicrostatin (VCN) was fused to an elastin-like polypeptide (A192). A significant fraction of fusion proteins self-assembled into multimers with a hydrodynamic radius of 15.9 nm. The A192-VCN fusion proteins compete specifically for cell-surface integrins on human umbilical vein endothelial cells (HUVECs) and two breast cancer cell lines, MDA-MB-231 and MDA-MB-435. Confocal microscopy revealed that, unlike linear RGD-containing protein polymers, the disintegrin fusion protein undergoes rapid cellular internalization. To explore their potential clinical applications, fusion proteins were characterized using small animal positron emission tomography (microPET). Passive tumor accumulation was observed for control protein polymers; however, the tumor accumulation of A192-VCN was saturable, which is consistent with integrin-mediated binding. The fusion of a protein polymer and disintegrin results in a higher intratumoral contrast compared to free VCN or A192 alone. Given the diversity of disintegrin proteins with specificity for various cell-surface integrins, disintegrin fusions are a new source of biomaterials with potential diagnostic and therapeutic applications.

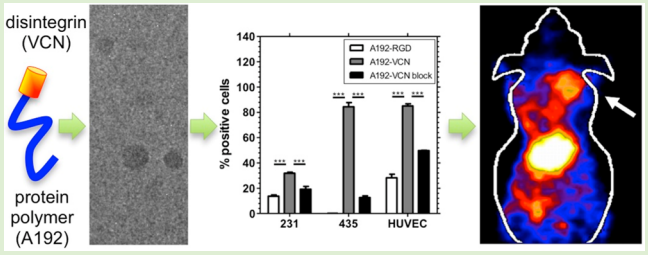

INTRODUCTION

Targeting tumor angiogenesis for drug delivery has been identified as a promising approach for three main reasons:[1] (i) angiogenesis is a common and genetically stable characteristic of most solid tumors; (ii) the tumor vasculature is readily accessible from the bloodstream; (iii) neovasculature can be targeted by RGD-containing peptides that bind to specific integrins. For example, the integrin $\alpha_v\beta_3$ is poorly expressed on quiescent endothelium and is selectively overexpressed on activated endothelial cells of growing vessels.[2,3] Overexpression of $\alpha_v\beta_3$ correlates with tumor progression and poor prognosis.[4−6] The RGD peptide is the dominant model for targeting vascular integrins. Through competitive inhibition, some of these peptides even induce apoptosis and inhibit angiogenesis.[3,7]

A source of naturally occurring high affinity ligands for integrins is found in the family of proteins known as disintegrins. These small (40−100 amino acids), cysteine-rich polypeptides were first isolated from viper venoms, which include contortrostatin (CN). Homologous domains are a part of the family of human ADAM (A disintegrin and metalloproteinase) proteins.[8,9] Many disintegrins contain the RGD

Received: November 4, 2013
Revised: May 24, 2014
Published: May 28, 2014

Table 1. Recombinant Proteins Evaluated in This Study

name	amino acid sequence*	MW (kDa)	construct
VCN	DAPANPCCDAATCKLTTGSQCADGLCCDQCKF MKEGTVCRRARGDDLDDYCNGISAGCPRNPHKGPATY	7.1	small protein
A192	G(VPGAG)$_{192}$Y	73.6	unimeric
A192-RGD	G(VPGAG)$_{192}$YRGDGG	74.0	unimeric
A192-VCN	G(VPGAG)$_{192}$ DAPANPCCDAATCKLTTGSQCADGLCCDQCKFMKEGTVCRRARGDDLDDYCNGISAGCPRNPHKGPATY	80.7	multimeric

*Bold: ELP guest residue; Underline: Arg-Gly-Asp consensus tripeptide.

or KGD peptide sequence, which target integrins involved in the aggregation of activated platelets.[10,11] Correct folding of disintegrins is important for their biological activity. Their proper folding depends on the appropriate pairing of 8−14 cysteine residues by disulfide bridges, which maintains the RGD-containing loop in its most active conformation.[12] Unlike free RGD peptides, the disintegrin specificity and affinity is enhanced by the tertiary structure of the disulfide framework and the amino acid chain at the carboxy terminus of the disintegrin.[8,13−15]

Although the pharmacological properties of the disintegrin CN have made it an intriguing molecule for potential anticancer therapeutic strategies,[16,17] it is produced in small quantities from snake venom (~0.01%). To overcome this obstacle, a recombinant disintegrin was designed by the Markland laboratory, vicrostatin (VCN), which can be produced through heterologous expression in *E. coli*.[18] VCN is antiangiogenic with significant anticancer activity, as demonstrated in murine models of human breast and prostate cancer.[18] VCN is as active as native CN in vitro and in vivo and has a higher affinity for integrin $\alpha_5\beta_1$, which is overexpressed on angiogenic endothelial cells.[18,19] Unfortunately, with their low molecular weight, small peptides like disintegrins are potentially challenging to formulate due to their rapid renal clearance.[16] For other therapeutic peptides, pharmacokinetics may be dramatically improved by through the use of macromolecular carriers.[20−22] Previously Swenson et al. determined the circulatory half-life of CN and liposomal CN, and it was observed that liposomal CN is cleared slowly compared to "naked" CN with a circulatory half-life of 19 and 0.5 h, respectively.[16]

As an alternative to conventional macromolecular carriers, protein polymers are under investigation for transport and delivery of imaging and therapeutic agents.[23−25] These bioconjugates are typically large hydrophilic molecules linked to a therapeutic agent, which can target tumors either passively through enhanced permeability and retention or actively through affinity toward a molecular target. Composed of repeat units of natural or unnatural amino acids, protein polymers have emerged as a promising new class of biomaterials.[26,27] Elastin-like polypeptides (ELPs) are protein polymers derived from a structural motif found in mammalian elastin and have sequence-dependent phase behavior that may be useful to control their disposition in the body.[28] ELPs consist of a five amino acid repeat (Val-Pro-Gly-Xaa-Gly)$_l$, where Xaa and l determine their phase behavior. When the temperature is raised above their transition temperature (T_t), they undergo a sharp (2−3 °C range) phase transition, leading to the coacervation of the biopolymer.[28,29] This process is fully reversible when the temperature is lowered and can be used to efficiently purify these materials. Below their T_t, ELPs remain highly water-soluble and have potential applications as biodegradable drug carriers.[30]

Here we report that the fusion of a recombinant disintegrin (VCN) to a high molecular weight ELP retains integrin-binding properties with an IC_{50} 30-fold lower than a control ELP fused to a linear RGD. Unlike low molecular weight VCN, these fusion proteins are well above the renal filtration cutoff, which reduces their renal clearance. A192-VCN retains its specificity for integrins expressed on human umbilical vein endothelial cells (HUVECs); furthermore, they retain this specificity in vivo.

MATERIALS AND METHODS

HUVECs were purchased from PromoCell GmbH (Heidelberg, Germany) and cultured in EC growth medium containing low serum (2%) and EC growth supplements (PromoCell). MDA-MB-231 and MDA-MB-435 cell lines were purchased from the American Type Culture Collection and grown in Dulbecco's Modified Eagle Medium (DMEM, Gibco) supplemented with 10% (v/v) fetal bovine serum. All cells were maintained at 37 °C under an atmosphere containing 5% carbon dioxide.

Recombinant Synthesis of ELP Protein Polymers. A synthetic oligonucleotide containing the vicrostatin (VCN) and the RGD peptide sequence was designed and inserted via cassette mutagenesis into the pET25b(+) cloning vector (Table 1). To facilitate insertion of the ELP sequence, the following plasmid reconstruction strategy was employed.[31] Two cloning vectors, one of which contained the ELP gene and another that contained the targeting sequence, were cut with two separate sets of restriction enzymes. The ELP vector was digested with BssHII and AcuI, while BssHII and BseRI were used to digest the second vector. The two sets of cut vectors were gel purified and ligated together using T4 DNA ligase (Invitrogen, Carlsbad, CA), generating the ELP-fusion protein indicated (Table 1). Gene sequences encoding for the desired polypeptides were confirmed using diagnostic DNA digestion and DNA sequencing from both 5′ and 3′ end of the open reading frame.

Protein Purification by Inverse Transition Cycling. pET25b-(+) expression vectors containing the desired constructs were transformed into *E. coli* origami B(DE3) competent cells for protein hyperexpression, and proteins were purified by inverse transition cycling (ITC).[32] Briefly, the bacteria were grown overnight in 50 mL of TB dry medium supplemented with ampicillin in an orbital shaker at 37 °C. Bacteria were centrifuged down and the pellet was resuspended in 1 L TB dry medium and cultured for 24 h in a 37 °C shaking incubator. The cultures were collected by centrifugation and resuspended in cold PBS. The proteins were liberated from bacteria by periodic probe-tip sonication. Insoluble debris was collected by centrifugation for 15 min at 4 °C, 12000 rpm, and the supernatant was transferred to another tube. Excess polyethylene imine (MW = 3000) was added to precipitate nucleic acids and the solution was centrifuged. The supernatant, containing soluble ELP, was heated to 37 °C to induce phase separation, and the coacervate was collected by centrifugation. The ELP was then resuspended in cold PBS and centrifuged at 4 °C again, completing one round of ITC. A total of 4−6 rounds of ITC were completed, sufficient to ensure the purity indicated (Figure 1a). Yields ranged from 50 to 100 mg per liter of bacterial culture. Both with and without a reduction by β-

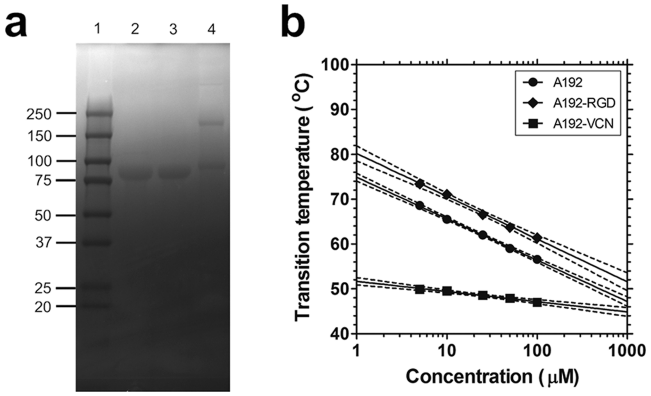

Figure 1. Fusion to a disintegrin reduces the ELP transition temperature. (a) Purified fusion proteins were evaluated for identity and purity using SDS-PAGE and stained with copper chloride. Lane 1: ladder; lane 2: A192; lane 3: A192-RGD; lane 4: A192-VCN. (b) The temperature−concentration phase diagram for the three ELPs were obtained using optical density at 350 nm. The best-fit line to the equation $T_t = m \ln[C] + b$ is shown (solid) along with 95% CI lines (dashed). The slope m was estimated as 4.08, 4.05, and 0.98 °C/ln[μM] for A192, A192-RGD, and A192-VCN, respectively. The intercept b was estimated as 80.0, 75.0, and 51.8 °C for A192, A192-RGD, and A192-VCN, respectively.

mercaptoethanol, the samples were resolved by SDS-PAGE (Lonza, Rockland, ME) and gels were negatively stained with copper chloride. The SDS-PAGE gel was scanned with a Molecular Imager Gel Doc XR System (Bio-Rad, Hercules, CA) and analyzed with Quantity One software (Bio-Rad). The concentration for ELPs was estimated using their absorbance at 280 nm according to molecular extinction coefficients of 1280 and 3760 M^{-1} cm^{-1} for A192/A192-RGD and A192-VCN/VCN, respectively.[42]

Phase Behavior Characterization of ELPs. ELP biomaterial phase separate above a transition temperature as a function of temperature and concentration. To ensure that both ELPs and ELP-fusions remain soluble at physiological temperatures, their transition temperatures were determined by optical density. Purified solutions in phosphate buffered saline (PBS) were heated at 1 °C/min in a multicell holder of a UV visible spectrophotometer (DU800 Spectrophotometer, Beckman Coulter, CA, U.S.A.). For the purposes of this manuscript, the transition temperature (T_t) was defined as the point of one-half maximal turbidity.

Size Exclusion Chromatography and Dynamic Light Scattering. Hydrodynamic radii for each construct were measured using bulk dynamic light scattering (DLS), size-exclusion chromatography (SEC), and size exclusion chromatography/dynamic light scattering (SEC-DLS). Bulk DLS was performed on a Dynapro plate reader (Wyatt Technology Inc., Santa Barbara, CA, U.S.A.). A total of 25 μM of polypeptide in phosphate buffered saline (PBS), pH 7.4, was measured at 37 °C. Before analysis, the solutions were filtered through Whatman Anotop filters with a 0.02 μM pore size and centrifuged to remove air bubbles. While the distribution of the particle populations is depicted in the figure, the reported errors in the text represent the standard error of the mean of three measurements.

Size exclusion chromatography was performed at 4 °C using a HiPrep 16/60 column (GE Healthcare Bio-Sciences, Piscataway, NJ, U.S.A.) with Sephacryl S-300 HR media connected to a Bio Rad Biologic DuoFlow chromatography system (Bio Rad Laboratories, Hercules, CA, U.S.A.). A192-VCN was loaded on the column equilibrated with phosphate buffered saline (PBS), pH 7.4. Elution was carried out isocratically with a flow rate of 1 mL/min and detection at 280 nm.

SEC-DLS was performed by diluting concentrated stocks of each construct to 15 mg/mL in PBS, pH 7.4, and filtering with a 0.2 μm filter, followed by SEC on an AKTA micro chromatography system (GE Healthcare Bio-Sciences) equipped with a Superose 6 10/300 column (GE Healthcare Bio-Sciences) at a flow rate of 0.5 mL/min. DLS was performed using a downstream Dawn-HELEOS, and differential refractive index (dRI) was monitored with a Optilab r-EX (Wyatt Technology Inc.).

Transmission Electron Microscopy (TEM) of A192-VCN Multimers. Cryogenic TEM imaging was performed on a Tecnai 12 TWIN Transmission Electron Microscope (FEI, Hillsboro, OR, U.S.A.), operating at 100 kV. A total of 5 μL of A192-VCN solution was placed on a holey carbon film supported on a copper TEM grid (Electron Microscopy Services, Hatfield, PA). All TEM grids used for cryo-TEM imaging were treated with air plasma to render the lacey carbon film hydrophilic. A thin film of the sample solution was produced using a Vitrobot with a controlled humidity chamber (FEI). After loading of the sample solution, the lacey carbon grid was blotted using preset parameters and plunged instantly into a liquid ethane reservoir precooled by liquid nitrogen. The vitrified samples were then transferred to a cryo-holder and cryo-transfer stage that was cooled by liquid nitrogen. To prevent sublimation of vitreous water, the cryo-holder temperature was maintained below −170 °C during the imaging process.

For negative contrast TEM, 5 μL of sample was spotted on a carbon film copper grid with 400 square mesh (Electron Microscopy Sciences, Hatfield, PA, U.S.A.) and the excess was removed with filter paper to leave a thin film of sample on the grid. After letting the sample dry for 10 min, 5 μL of 2% uranyl acetate was added to sample grid, and the excess was removed after 10 s. All samples were dried for at least 2 h before TEM imaging. All images were recorded by a SIS Megaview III wide-angle CCD camera (Olympus Soft Imaging Solutions, Münster, Germany).

Fluorescence Activated Cell Sorting (FACS) Analysis. Cellular binding of the ELP, ELP-fusion protein, and disintegrin were analyzed by FACS. For quantification, ELP and ELP-fusion proteins were labeled with *N*-hydroxysuccinimide rhodamine (Thermo Scientific, Rockford, IL) and purified using a PD-10 desalting column (GE Healthcare Bio-Sciences). VCN was labeled with fluorescein thiocyanate (FITC) using the EZ-label FITC labeling kit (Pierce Biotechnology, Rockford, IL) according to the manufacturer's instructions. Unlabeled or excess FITC molecules were removed by centrifuging the samples with a 3K MWCO filter (Corning Inc., Corning, NY). An Alexafluor 488-labeled LM609 antibody (Millipore, MA) was used to stain the integrin $\alpha_v\beta_3$. Cells (4×10^5) were seeded on a 12-well plate and incubated overnight at 37 °C under 5% carbon dioxide. Cells were washed with Dulbecco's Phosphate Buffered Saline (DPBS), and DMEM was replaced. A total of 25 μM of rhodamine-labeled protein was added to the cells and incubated for 2 h. Cells were detached with trypsin-EDTA (0.05% trypsin, 0.5 mM EDTA pH 8.0) and suspended in DPBS containing 1% BSA. A total of 1×10^4 cells were analyzed for fluorescence using a FACScan (Becton Dickinson, San Jose, CA). Nontreated or rhodamine-labeled ELP (A192) treated cells were used as negative controls. For blocking studies, 50 μL (10 mg/mL) of VCN was incubated with the cells for 30 min. VCN was removed, and the cells were washed with DPBS. Media was replaced and 25 μM of rhodamine-labeled ELPs were incubated for another 1.5 h.

Confocal Microscopy. HUVECs (2×10^5) were plated on coverslips coated with fibronectin in 12-well plates and cultured for 48 h. Rhodamine-labeled ELP and ELP-fusion protein (25 μM) were added to the cells and incubated for 1 h at 37 °C in a humidified 5% CO_2 atmosphere. To block the ELPs, a blocking dose of unlabeled VCN (50 μL of 10 mg/mL) was added for 30 min before addition of the labeled ELP-fusion. Following incubation, cells were washed with DPBS and fixed with 4% paraformaldehyde in DPBS at room temperature for 15 min. Nuclear staining was performed by adding Hoescht 33285. Fluorescence images were acquired with a laser scanning confocal microscope (Zeiss LSM 510 Meta, Thornwood, NY) equipped with argon and HeNe lasers.

Cell-Surface Integrin Binding Assay. In vitro integrin affinity and specificity were assessed via displacement of ^{125}I-echistatin (GE Healthcare Bio-Sciences) as the integrin specific radioligand.[33] Experiments were performed on $\alpha_v\beta_3$ positive MDA-MD-435 human

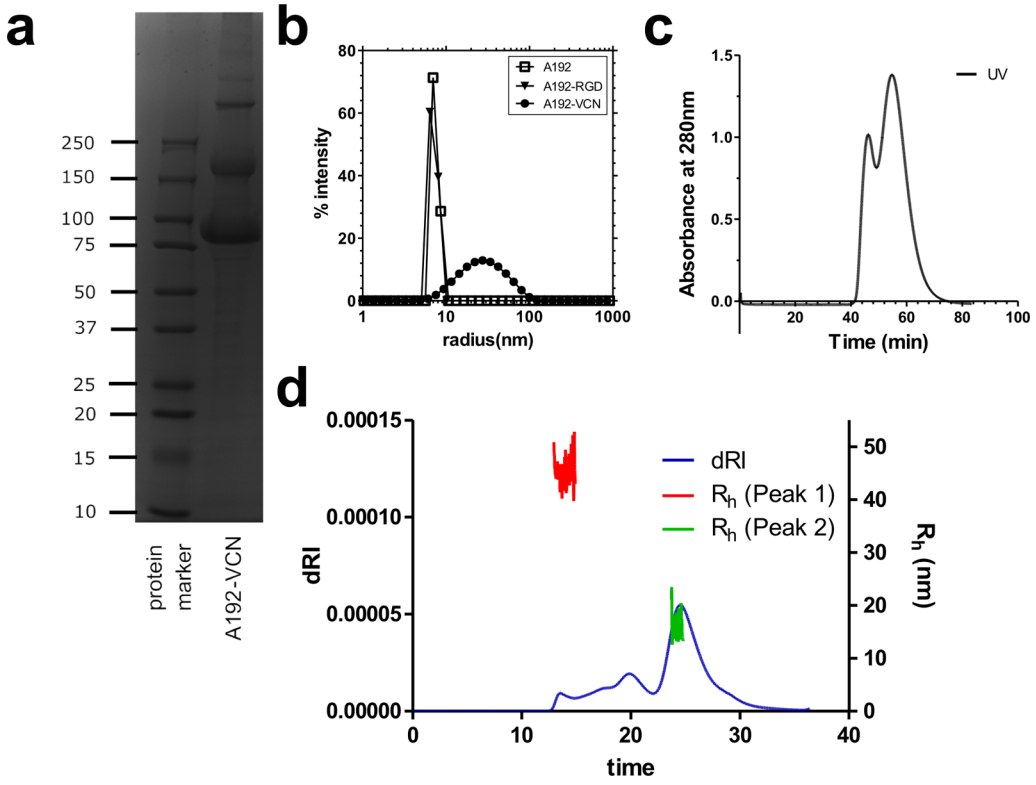

Figure 2. Disintegrin ELP fusion forms multimeric structures with increased hydrodynamic radius. (a) Purified A192-VCN was run on a nonreducing SDS-PAGE gel and stained with copper chloride, showing assembly of varying numbers of A192-VCN monomers. Lane 1: ladder; Lane 2: A192-VCN. (b) Batch DLS measurements of A192 (open squares), A192-RGD (triangles), and A192-VCN (circles) in PBS, pH 7.4. This trace indicates the presence of a significant population of multimers in the A192-VCN sample. (c) UV trace of SEC run of A192-VCN, indicating two dominating populations of construct sizes. (d) SEC-DLS results for A192-VCN, where dRI trace (blue) confirms two populations. The first peak (red) reflects a larger aggregate with a hydrodynamic radius of 45.7 nm and the second peak (green) reflects a smaller multimer with a hydrodynamic radius of 15.9 nm. The R_h for both peaks is significantly larger than that observed for A192 and A192-RGD.

breast cancer cells cultured in DMEM (Life Technologies, Carlsbad, CA) with 10% FBS. During the assay, the cells were harvested, washed twice with PBS, and resuspended (2×10^6 cells/mL) in binding buffer (25 mM Tris, 150 mM NaCl, 1 mM $CaCl_2$, 1 mM $MgCl_2$, 1 mM $MnCl_2$, 0.1% BSA, pH 7.4). Filter multiscreen DV plates (96-well; pore size, 0.65 μm; EMD Millipore, Billerica, MA, U.S.A.) were seeded with 10^5 cells and incubated with ^{125}I-echistatin (100 pM/200 μL) in increasing concentrations of ELPs and RGD peptide analogues (0–10000 nM). After 2 h at room temperature, the plates were filtered through a multiscreen vacuum manifold and washed twice with cold binding buffer. The hydrophilic polyvinylidenedifluoride (PVDF) filters were collected and the radioactivity was determined using a gamma counter. Experiments were performed with triplicate samples. The best-fit 50% inhibitory concentration (IC_{50}) values were calculated by nonlinear regression using GraphPad Prism (GraphPad Software, Inc.).

Orthotopic Xenograft of Human Breast Cancer Model. All animal experiments were performed in compliance with the guidelines established by the USC Institutional Animal Care and Use Committee. MDA-MB-231, a human breast cancer cell line, was suspended in DMEM and 10% matrigel, and injected into the right mammary fat pad at 2.5×10^6 cells per athymic nude mouse (Harlan Laboratories, Indianapolis, IN) and allowed to grow for 2 weeks before imaging.

Chelation and Radiolabeling Proteins with the Positron Emitter, ^{64}Cu. Two chelation strategies were used to characterize proteins by microPET imaging. The first chelator, 1,4,7,10-tetraazacyclododecane-1,4,7,10-tetraacetic acid (DOTA), was activated by ethylenediaminetetraacetic acid (EDC) and *N*-hydroxysulfosuccinimide (SNHS) at pH 5.5 for 30 min (4 °C), with molar ratio of DOTA/EDC/SNHS (10:5:4). Then, 5 equivalent of activated DOTA were mixed with proteins in borate buffer (0.1 M, pH 8.5). The reaction was incubated at 4 °C overnight. Size-exclusion chromatography was performed using a PD-10 column (GE Healthcare Bio-Sciences) to remove unreacted DOTA-NHS.

A second chelator, AmBaSar, was explored to reduce the nonspecific loss of copper ions.[34] AmBaSar was activated by EDC and SNHS at pH 4.0 for 30 min (4 °C) with a molar ratio of AmBaSar/EDC/SNHS = 10:9:8. Then, 5-fold molar excess of activated AmBaSar was mixed with the protein polymer in borate buffer (0.1 M, pH 8.5). The reaction was kept at 4 °C overnight. Size-exclusion PD-10 chromatography was used to remove unreacted reagents from the protein polymer. The DOTA and AmBaSar conjugates were labeled with ^{64}Cu by addition of 1 mCi of ^{64}Cu (10 nmol protein per mCi ^{64}Cu) in 0.1 N ammonium acetate (pH 5.5) buffer followed by 45 min incubation at 40 °C. Before purifying the ^{64}Cu-proteins using a PD-10 column, diethylene triamine pentaacetic acid (DTPA; 3 μL, 10 mM, pH 6.02) was added to remove ^{64}Cu that weakly interacts with the peptide backbone.

MicroPET Imaging of Disintegrin Protein Polymer Fusions. Molecular imaging was performed using a microPET R4 rodent model scanner (Concorde Microsystems, Knoxville, TN). Mice were injected with ~100–150 μCi ^{64}Cu-labeled samples via the tail vein. For imaging, the mice were anaesthetized with 2% isofluorane and placed near the center of the field of view, where the highest resolution and sensitivity are obtained. Static scans were obtained at 0.5, 2, 4, 24 and 48 h post-injection. The images were reconstructed by a two-dimensional ordered subset expectation maximum (2D-OSEM) algorithm.

RESULTS

Characterization of A192-VCN. A vector encoding the VCN sequence was fused to an ELP gene called A192, which

has l = 192 and Xaa = Ala (Table 1). Purification of the ELPs by inverse transition cycling yielded proteins of good purity, which were characterized using SDS-PAGE under reducing conditions (>95%; Figure 1a). While the major species observed for A192-VCN was monomeric and consistent with the expected molecular weight, some higher order multimers were visible. A possible explanation for these dimers and trimers is that intermolecular covalent bonds bridge the amino acid sequence on the VCN domains. Unlike the VCN domain, the length of the A192 ELP is relatively inert, as it lacks any hydroxyl, acid, thiol, or aromatic functional groups. The most likely explanation for these multimers is that they result from intermolecular cross-links between 1 or 2 of the 10 cysteine residues present on the VCN sequence. Typically, disintegrin cysteines form intramolecular bonds that rigidify the binding domain; furthermore, due to their high linear density, it is plausible these disulfides are less susceptible to standard reduction using β-mercaptoethanol. The observation of these multimers prompted us to further explore the physical-chemical properties for these fusion peptides.

To confirm that these temperature-dependent species remain soluble at physiological temperatures, their phase behavior was studied (Figure 1b). All constructs remain soluble until well above physiological temperatures. A192-RGD and A192 exhibited similar transition temperatures. In contrast, A192-VCN has a lower transition temperature. We recently reported that nanoparticles stabilized at their corona by an ELP with alanine guest residues similarly reduces the bulk transition temperatures.[35] Previous reports also show that the slope and intercept of the ELP phase diagram depend on the number of pentameric ELP repeats.[43] This raised the possibility of determining whether or not the ELP phase diagrams are consistent with the formation of multimeric species (unimer, dimer, trimer, tetramer, etc.). Prior characterization of an ELP library with Xaa = Ala revealed a fit by multiple linear regression as follows:[35]

$$T_t = 40.5 + \frac{7009}{l} - \frac{850.1\ \ln(C)}{l} \quad (1)$$

where T_t is the transition temperature [°C], l is the number of ELP pentamers, and C is the ELP concentration (μM). Based on inspection of eq 1, the apparent number of pentamers can be estimated from the intercept, $\underline{b}$ (1 μM), of the best-fit line (Figure 2b) as follows:

$$l_{\text{intercept}} = \frac{7009}{b - 40.5} \quad (2)$$

Alternatively, the apparent number of pentamers can be estimated from the slope, m, of the best-fit line (Figure 2b) as follows:

$$l_{\text{slope}} = \frac{850.1}{m} \quad (3)$$

Using eq 2, $l_{\text{intercept}}$ was estimated as 177, 203, and 620 pentamers for A192, A192-RGD, and A192-VCN, respectively. Similarly using eq 3, l_{slope} was estimated as 208, 210, and 864 pentamers for A192, A192-RGD, and A192-VCN, respectively. Based on sequencing and SDS-PAGE, each monomer contains 192 ELP repeats. As such the phase diagrams observed for native A192-VCN are consistent with that expected for trimers and tetramers. Conversely, A192 and A192-RGD phase diagrams are consistent with unimers. While these phase diagrams cannot independently confirm that A192-VCN is multimeric, they do show that the formation of trimers or tetramers may be sufficient to produce a phase diagram similar to that observed.

The evidence that A192-VCN forms low number multimers, prompted us to explore the structure of these assemblies in greater detail (Figure 2). First, SDS-PAGE under nonreducing conditions was used to reveal significant populations of disulfide-linked species ranging from dimers to hexamers (Figure 2a). Next, the sizes for these ELPs were characterized using batch dynamic light scattering (DLS) to identify the cumulant-fit average hydrodynamic radii, R_h (25 μM, 37 °C), of 7.8 ± 1.2, 7.1 ± 0.8, and 22.3 ± 5.3 nm for A192, A192-RGD, and A192-VCN, respectively (Figure 2b). Consistent with multimerization, native A192-VCN exhibited an R_h much larger than A192 or A192-RGD alone. Thus, the most reasonable explanation for multimerization is that that the VCN portion of the fusion protein self-associates. This is consistent with the observation that native disintegrins are commonly identified as dimeric species. While it appears that covalent disulfide cross-links may be involved in multimerization, data presented here cannot rule out the possibility that the VCN also undergoes noncovalent self-association. Due to the limitations of batch DLS to distinguish particles of similar size, size exclusion chromatography (SEC) was used to investigate the dominant species.

Due to the apparent formation of A192-VCN multimers as determined by DLS and SDS-PAGE, SEC was used to resolve populations present in the sample (Figure 2c). UV−vis spectroscopy revealed two populations with peak retention times of 46.4 and 54.8 min, which are consistent with two distinct hydrodynamic radii. To further characterize the identity of these peaks, in-line SEC-DLS was performed, which allows the determination of the hydrodynamic radius for each peak independently. SEC-DLS results (Figure 2d) revealed that the peaks have apparent hydrodynamic radii of 45.7 nm for the first peak, and 15.9 nm for the second peak, with the two peaks comprising 29.9 and 70.1% of sample weight, respectively. This mixture of hydrodynamic radii are consistent with that observed by batch DLS (22.3 nm), which is an average of the two populations skewed by abundance, particle size, and polydispersity. Importantly, even the late-eluting peak (15.9 nm) had a hydrodynamic radius much larger than for a monomeric A192 (7.1 nm). Thus, the first peak appears to be a less abundant aggregate, while the second peak with a smaller hydrodynamic radius we define as a multimer.

The structure of these multimers was further confirmed by transmission electron microscopy. Cryo-TEM of A192-VCN revealed the presence of spherical structures with an average radius of 14 ± 2.2 nm (Figure 3a), which is in agreement with the major population observed by SEC-DLS. Due to its higher abundance and smaller radius, cryo-TEM revealed only the smaller species consistent with multimers. The absence of the larger aggregates in cryo-TEM may result from the preparation of a thin layer of vitrified water required to obtain contrast for the small particles. Negative contrast TEM did reveal a similar population of ∼15 nm radius particles that partially aggregate into larger clusters during drying (Figure 3b). These larger populations would also be consistent with larger aggregates observed by SEC. Despite this, both TEM approaches revealed a dominant species of multimers 15 nm in radius, which is in close agreement to the major species revealed by both batch DLS and SEC-DLS.

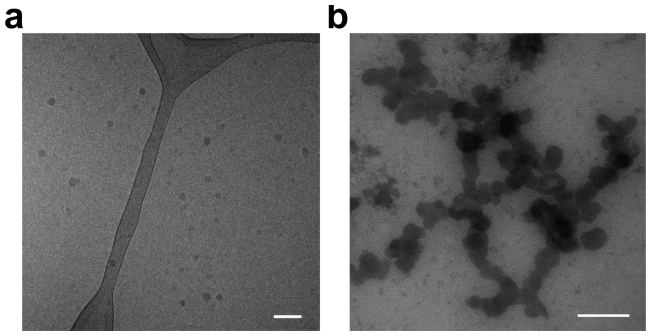

Figure 3. A192-VCN multimers have spherical morphology. (a) CryoTEM of A192-VCN and (b) negative stain TEM of A192-VCN both demonstrate nanostructures with radii of ~15 nm with a relatively narrow distribution of morphologies and are consistent with the observed hydrodynamic radius of multimers from SEC-DLS (15.9 nm). The negative TEM reveals the presence of aggregates of these particles, which may be an artifact of drying. The scale bar represents 100 nm.

Having established that the A192-VCN fusion assembles into small multimeric particles, we next explored their ability to specifically associate with pro-angiogenic integrins. An α_v integrin competition assay was performed using ^{125}I-echistatin and the α_v integrin−positive cell line MDA-MB-435. This assay tests specificity of molecules for cell-surface α_v integrins by their ability to displace a commercially available α_v-binding disintegrin, called echistatin. Except for A192, all of the peptides competed for echistatin to varying degrees in a concentration dependent manner (Figure 4). The IC_{50} values estimated for VCN, A192-VCN, and A192-RGD were 0.48 ± 0.14, 1.64 ± 0.33, and 51.8 ± 44.3 μM, respectively.

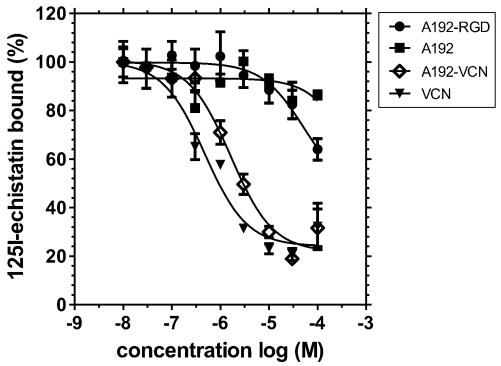

Figure 4. A192-VCN displaces echistatin with comparable affinity to VCN. A192 (squares), A192-RGD (circles), A192-VCN (open diamonds), and VCN (triangles) were compared for their ability to displace a commercial disintegrin, ^{125}I-echistatin, from the surface of $\alpha_v\beta_3$ integrin positive MDA-MB-435 cells. A192-VCN has an IC_{50} similar to that of free VCN, with A192 and A192-RGD displaying significantly higher IC_{50}s.

Expression of the $\alpha_v\beta_3$ Integrin across Primary and Transformed Cell Lines. To evaluate the expression of $\alpha_v\beta_3$ integrins, flow cytometric analysis of MDA-MB-231, MDA-MB-435, and HUVEC was carried out using an anti-α_v integrin antibody. The surface density of $\alpha_v\beta_3$ integrins and binding of FITC-VCN in each cell line were significantly different with the pattern of integrin expression levels HUVEC > MDA-MB-435 > MDA-MB-231 (Supporting Information, Figure S1). Relatively low binding of VCN to 231 and 435 cells were exhibited; however, an ~6-fold increase in signal from the control was observed for HUVEC cells. These data are consistent with the selection of these cell lines for targeting using multimers of A192-VCN.

Quantitative Uptake of Fusion Proteins by Flow Cytometry Analysis. Flow cytometry was used to determine the specific uptake of ELP-fusion proteins by endothelial cells (HUVEC) and breast cancer cell lines with moderate (MDA-MB-231) and high (MDA-MB-435) affinity for VCN. Figure 5a−c show the cellular uptake of rhodamine-labeled ELPs after

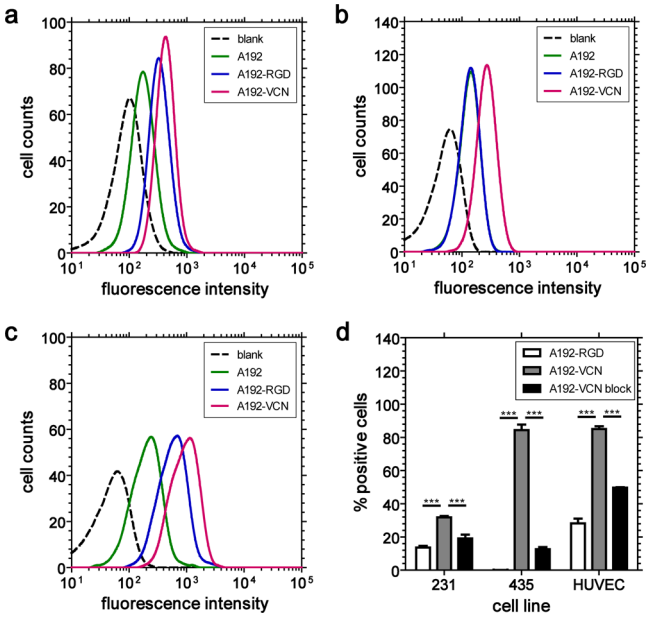

Figure 5. A192-VCN undergoes receptor-mediated binding in primary and transformed cell lines. Cell-surface binding was assessed for ELP constructs incubated with endothelial (HUVEC) and breast cancer cell lines (MDA-MB-231 and MDA-MB-435). Cells were incubated for 2 h at 37 °C with 25 μM of rhodamine-labeled A192, A192-VCN, and A192-RGD. The representative histogram from (a) MDA-MB-231, (b) MDA-MB-435, and (c) HUVEC shows that A192-VCN binds as well or better than A192 or A192-RGD controls. Dashed lines indicate untreated cells. (d) The percentage of positive cells undergoing integrin specific binding were gated with respect to A192 treated cells (nonspecific control). To confirm that the binding of A192-VCN is receptor specific, cells were blocked by preincubation for 30 min at 37 °C with (50×) excess with unlabeled free VCN prior to the addition of rhodamine-labeled A192-VCN. Results are mean ± SD, $n = 3$ (**$p < 0.05$, ***$p < 0.01$).

cells were incubated for 2 h at 37 °C. Each cell line showed minimal nonspecific association with A192; however, A192-RGD and A192-VCN bind at a much higher level. In each cell line, A192-VCN exhibits the largest increase in binding. To quantify this data, the percentage of positive cells that specifically bind the fusion protein, relative to the nonspecific binding of the negative control (A192), was gated for each cell type (Figure 5d). Within each cell type, a differential pattern of cell binding was observed. When treated with monomeric A192-RGD, the HUVECs exhibited the highest percentage of bound cells, followed by the MDA-MB-231 cells and MDA-MB-435 cells. A one-way ANOVA revealed significant differences in binding of A192-RGD between all cell groups ($p < 0.05$). A similar binding pattern was exhibited for A192-VCN. When comparing between treatment groups in the same cell

dx.doi.org/10.1021/bm401622y | Biomacromolecules 2014, 15, 2347−2358

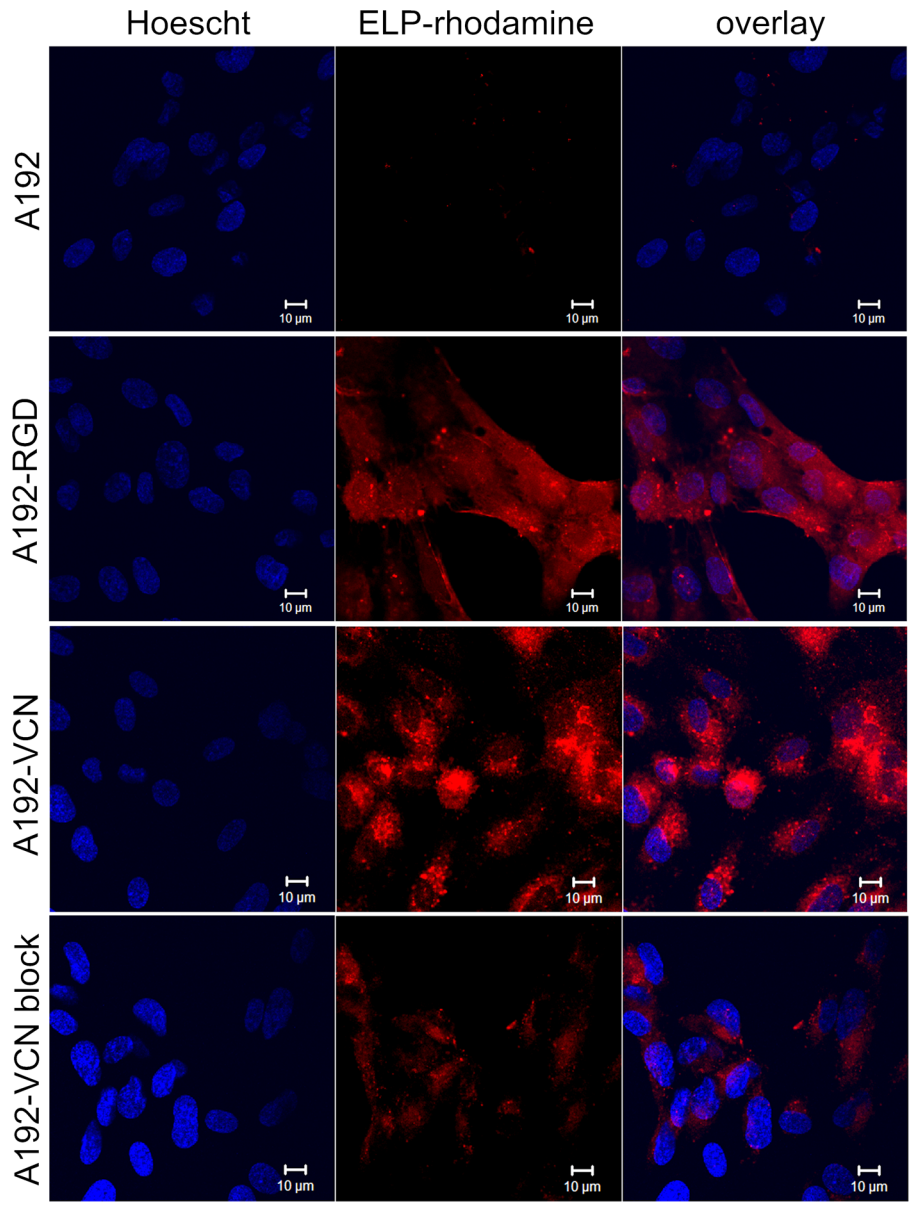

Figure 6. A192-VCN internalizes into a primary endothelial cell culture via a saturable process. Confocal microscopy was used to assess HUVECs incubated with 25 μM A192, A192-RGD, and A192-VCN labeled with rhodamine for 1 h at 37 °C. A blocking study was also performed by preincubation with (50×) excess free VCN for 30 min before adding rhodamine-labeled A192-VCN. Cells were fixed with 4% paraformaldehyde and incubated with Hoescht for nuclear staining.

line, A192-VCN treated produce a higher percentage of positive cells than A192-RGD. This difference is significant across all cell types ($p < 0.001$). To characterize the specificity of the A192-VCN for the integrins targeted by free VCN, a blocking experiment was also performed (Figure 5d). Blocking with excess VCN reduces the percentage of cells positive for A192-VCN in all cell lines. Up to 70% inhibition was observed for both the 231 ($p < 0.0001$) and 435 ($p < 0.0001$) cells. Blocking was slightly less effective in HUVECs; however, the decrease in cells positive for A192-VCN remained statistically significant ($p < 0.0001$).

Internalization and Intracellular Distribution of Fusion Protein. α_v positive endothelial cells are the most likely candidates for interaction with A192-VCN multimers in vivo; therefore, confocal laser scanning microscopy was used to confirm cellular uptake by HUVECs (Figure 6a). In confirmation of the FACS study, there was minimal binding of A192; however, A192-RGD bound efficiently to the cellular surface. Similar to A192-RGD, A192-VCN had a high level of association; however, the punctate intracellular distribution pattern for A192-VCN hints at an enhanced level of cellular internalization (Figure 6). To confirm that uptake for A192-VCN was receptor dependent, excess VCN was used to block integrin-mediated binding. The A192-VCN blocking study shows nearly complete inhibition of association of A192-VCN to HUVECs (Figure 6). This suggests that A192-VCN specifically binds to similar integrins targeted by the parent disintegrin, VCN, which includes $\alpha_v\beta_3$ integrin. Overall, the results from confocal imaging studies are in agreement with the results obtained from flow cytometry (Figure 5) and confirm that A192-VCN is internalized into endothelial cells via heterodimeric integrins targeted by VCN and the RGD peptide alone.

dx.doi.org/10.1021/bm401622y | *Biomacromolecules* 2014, 15, 2347−2358

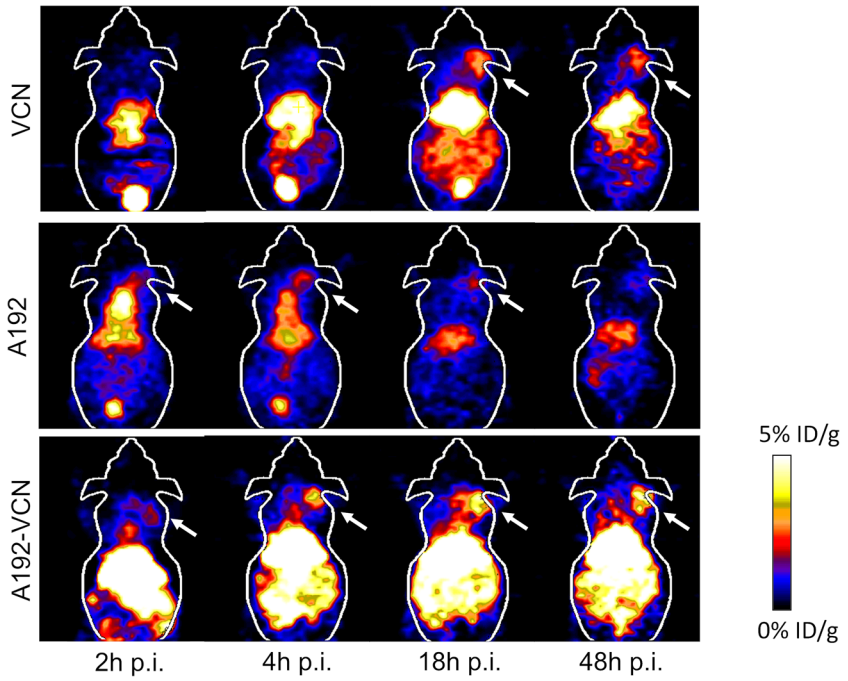

Figure 7. microPET imaging reveals that A192-VCN accumulates in an orthotopic model of human breast cancer. ^{64}Cu-DOTA-labeled proteins were administered systemically to mice carrying MDA-MB-231 tumors. Serial imaging was performed, and coronal images centered on the tumor for VCN, A192, and A192-VCN are depicted between 2 and 48 h post injection. A representative mouse is shown from each group (n = 3/group). Two major pools of blood are present in the heart (top) and liver (middle). At later time points, the gastrointestinal track (lower) and the bladder (bottom) enhance in contrast. The tumor locations are indicated by arrows.

Serial microPET Imaging of Fusion Protein Biodistribution. To determine if ELP stabilization has the potential to shift biodistribution patterns of VCN, the systemic biodistributions of VCN, A192, and A192-VCN were compared using microPET imaging (Figure 7). Constructs were followed for 48 h, a period of time during which the A192-VCN multimers maintain a stable hydrodynamic radius (Supporting Information, Figure S2). The macrocyclic chelator DOTA was used to label recombinant proteins and chelate the positron emitter, ^{64}Cu. Radiolabeled constructs were administered intravenously to nude mice bearing an orthotopic breast cancer model, MDA-MB-231. High levels of activity were observed in the heart from 2 to 4 h post-injection for A192 and A192-VCN, which suggests that they remain in circulation (Figures 7 and 8a). The heart and aortic arch contain a relatively large internal volume containing blood, which makes their intensity correlate with the blood concentration of the radiolabel. For free VCN, minimal signal was observed in the heart; furthermore, VCN signal rapidly accumulated in the bladder. This behavior is consistent with relatively rapid renal clearance expected for this small protein (7.1 kDa) as compared to the unmodified A192, the higher molecular weight ELPs (Table 1). While the heart signal completely disappears for A192 by 18 h, a significant heart signal remained for A192-VCN (Figures 7 and 8a).

In addition to slowing clearance of VCN, fusion to A192 produced an apparent enhancement in tumor accumulation compared to either A192 or VCN alone (Figures 7 and 8g). A192 was found at low levels in the tumor, consistent with passive targeting. While some tumor accumulation was observed for VCN, tumor intensity for A192-VCN was detected earlier and with greater intensity. These results suggest active targeting mediated by the VCN domain, which is facilitated by the large hydrodynamic radius for A192-VCN (Figure 2). In addition to tumor and heart accumulation, significant hepatic and intestinal signal was observed with the A192-VCN. Despite this intestinal staining, the ^{64}Cu/DOTA chelation strategy was adequate to visualize the heart, kidneys, bladder, and tumor, which were quantified using a region of interest (ROI) biodistribution (Figure 8).

By identifying key tissues through serial microPET imaging, ROIs were established in each mouse that enabled the quantification of tissue concentration as a function of time (Figure 8). ANOVA was used to compare the concentration of each construct at 4 h. First, the signal from the heart was evaluated, which can be used as a surrogate measure for the blood concentration (Figure 8a). The intensity in the heart suggests that A192 and A192-VCN remained in circulation after 4 h, but were entirely cleared by 48 h. For VCN, significantly lower signal was detected in the heart compared to either A192 (p = 0.002) or A192-VCN (p = 0.03). Minimal signal was observed in the muscle, where there was a slight difference between VCN and A192-VCN (p = 0.0283) at 4 h (Figure 8b).

Having observed that the signal intensity of VCN in the heart was lower than A192-VCN, the kidney and bladder concentrations were compared to determine if renal clearance may be responsible for the difference (Figure 8c). VCN exhibited the highest kidney uptake, which was significantly different from A192 (p = 0.0003) and A192-VCN (p = 0.03). Renal accumulation of VCN occurred rapidly and then declined during the study. A192 exhibited the lowest kidney accumulation of all the constructs (Figure 8c). Subsequent transfer from the kidneys to the bladder was observed (Figure 8d). The bladder accumulation of A192 was significantly less than that for VCN (p = 0.003). The different observed

dx.doi.org/10.1021/bm401622y | *Biomacromolecules* 2014, 15, 2347−2358

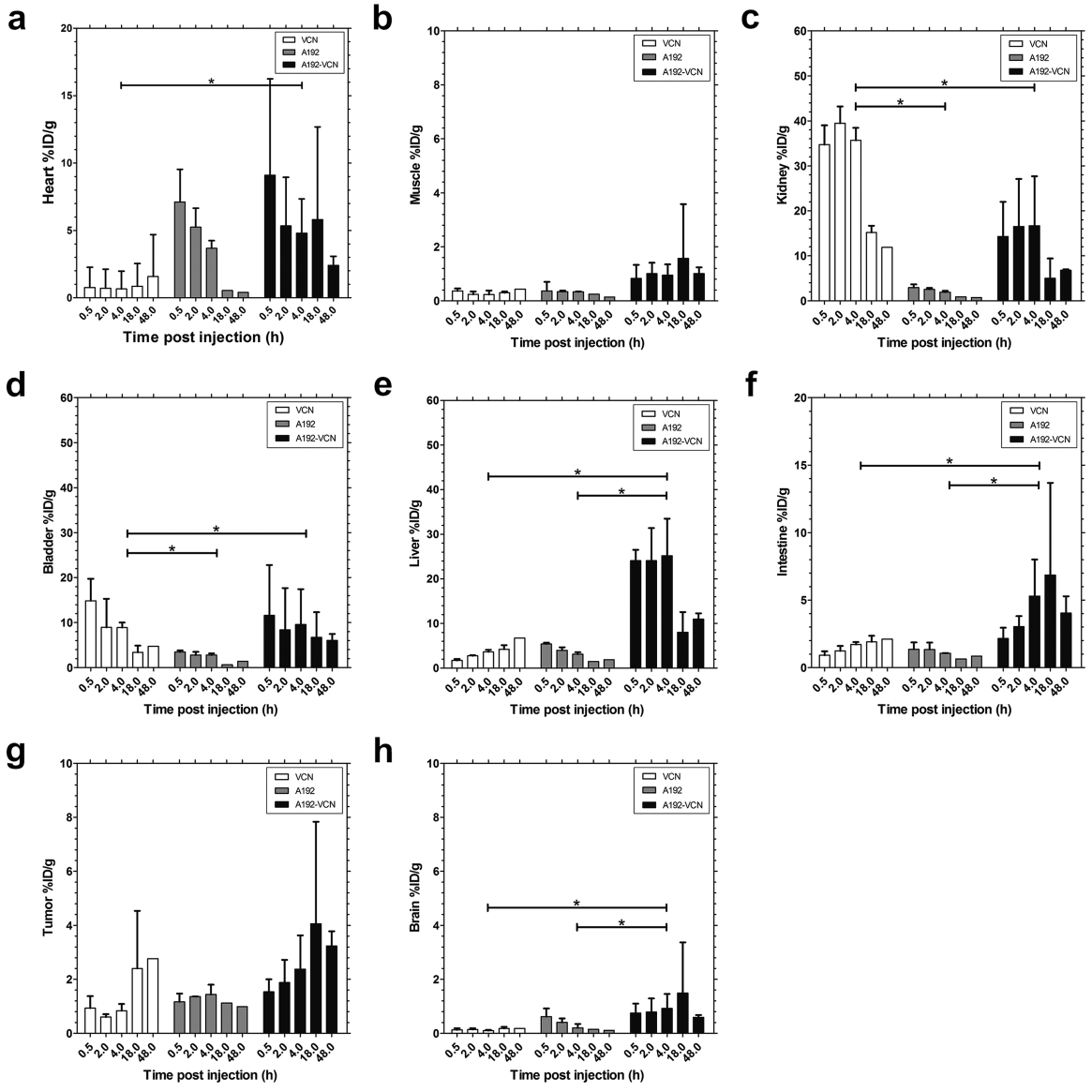

Figure 8. Fusion between A192 and the VCN disintegrin shifts the pattern of systemic biodistribution. ^{64}Cu-DOTA-labeled proteins (VCN, A192, and A192-VCN) were administered to athymic nude mice implanted with MDA-MB-231 tumors (n = 3). Serial images were quantified within the (a) heart, (b) muscle, (c) kidneys, (d) bladder, (e) liver, (f) intestine, (g) tumor, and (h) brain expressed as %ID/g calculated from ROI image analysis. Values indicate the mean ±95%CI.

intensities in the kidney are consistent with a reduction in renal clearance for VCN.

The most evident difference between A192-VCN and either A192 or VCN alone was the significant accumulation in the liver and intestines. The liver accumulation of A192 was not as high as the other constructs (Figure 8e). While the liver showed significantly higher uptake of A192-VCN at 4 h compared to A192 (p = 0.03) and VCN (p = 0.007), it subsequently decreased in intensity at 18 and 24 h. Simultaneously, signal from A192-VCN appeared in the intestinal tract (Figure 8f). This suggested that the ^{64}Cu/DOTA chelate (and its metabolic products) may undergo biliary excretion into the gastrointestinal tract.

Having demonstrated significant biodistribution effects relating to renal and hepatic clearance, the net effect on intratumoral accumulation was characterized (Figure 8g). Minimal tumor signal was observed for VCN up until 4 h, with a slight increase in signal at 18 and 48 h post-injection. For A192-VCN, a steady increase in accumulation was observed until 18 h post-injection, where it achieved 4.1% ID/g. All other tissues evaluated showed negligible uptake (Figure 8h). In summary, this biodistribution data shows that appending VCN to a macromolecular carrier may reduce renal clearance and favor hepatic clearance; however, the instability of the ^{64}Cu/DOTA signal upon hepatic uptake made it challenging to characterize the specificity of A92-VCN for intratumoral uptake.

A192-VCN Uptake Occurs by a Receptor-Mediated Process. Having characterized the serial biodistribution of the fusion protein, we explored the possibility that intratumoral (and systemic) accumulation is due to a saturable process, such as is expected for VCN-mediated binding to vascular integrins. To facilitate this study, an alternative chelating agent (AmBaSar) was used to carry the ^{64}Cu radioisotope, which has improved stability in vivo.[36] Representative images of tumor bearing mice with and without a preblocking injection of

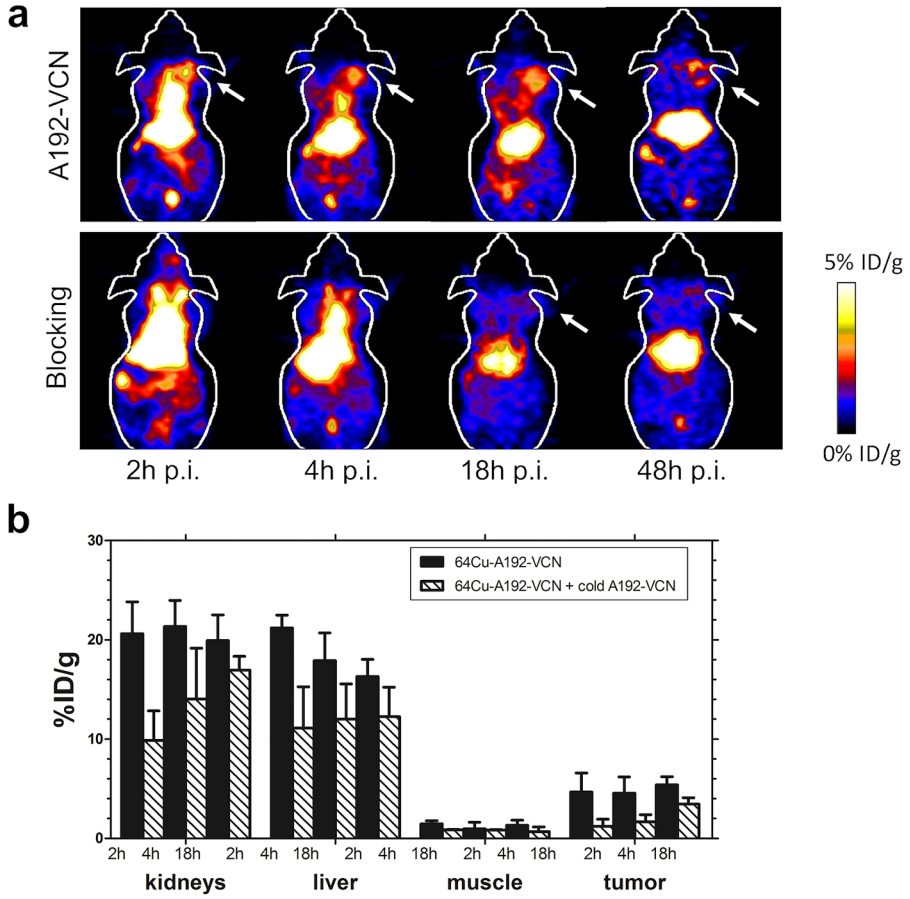

Figure 9. A192-VCN accumulation is saturated by preblocking with unlabeled fusion protein. An alternative chelator, ^{64}Cu-AmBaSar was used to evaluate constructs composed of A192-VCN in the absence or presence of a blocking dose of cold A192-VCN. (a) Coronal images of MDA-MB-231 tumor-bearing mice from 2 to 48 h post-injection (p.i.). (b) This blocking effect was quantified in several major tissues, including the kidneys, liver, and tumor. Values indicate the mean ± SD.

unlabeled A192-VCN clearly show reduced signal of the gastrointestinal tract (Figure 9a) compared to the ^{64}Cu/DOTA study (Figure 7). Accumulation in all tissues including the tumor at 4 h was reduced significantly reduced (p = 0.003) by blocking, which indicates that accumulation of A192-VCN is via a saturable process, which may be due to integrin binding specificity (Figure 9b). The uptake of radiolabeled fusion protein in other organs was also reduced, which has been observed for other RGD-mediated tracers.[37] This is in agreement with published results, as it has been reported that $\alpha_v\beta_3$ integrin imaging probes demonstrate low but blockable uptake in normal tissues.

DISCUSSION

As reported previously, the VCN disintegrin halts the growth of solid tumors through high affinity to and specific disruption of intratumoral integrins.[18] An obstacle to their clinical development, disintegrins are small peptides (7.1 kDa), which are below the renal filtration cutoff. As demonstrated by microPET imaging (Figure 7), VCN achieves only a moderate target-to-background ratio. This may be because rapid renal clearance minimizes the exposure of VCN to target tumor-associated vascular integrins. As confirmed in this report, free VCN is rapidly cleared from the blood to the kidney and bladder, which suggests efficient renal clearance (Figure 8). To address this problem, genetic engineering was used to append VCN to a 73.6 kDa protein polymer called A192. In a previous study comparing a lower molecular weight (37.0 kDa) protein polymer to A192, A192 had reduced renal clearance by 10-fold.[36] Most surprising is the discovery that these fusion proteins form a significant population of multimers that appear to be cross-linked by the cysteine-rich disintegrin domain. We postulate that intermolecular disulfides and also noncovalent intermolecular pairing between the disintegrin may drive their assembly; however, additional studies into the structure of these multimers are needed to investigate the nature of this assembly process.

Many classes of macromolecules with an appropriate hydrodynamic radius, resistance to opsonization, and long-elimination half-life accumulate in tumors via passive accumulation. For example, liposomes[38] and polymeric micelles[39] accumulate readily with or without target-mediated ligands; however, the question of whether uptake is specific for the intended target is not always addressed. Heneweer et al.[40] proposed that, to demonstrate target-mediated specificity, the intratumoral intensity should exceed the value observed for a nontargeted analogue and that this accumulation should respond to competition for the intended target. Thus, we have used both in vitro and in vivo methods to test both of these criteria for A192-VCN. The fusion protein containing the disintegrin sequence is potent at displacing echistatin from cell-surface $\alpha_v\beta_3$ integrins (Figure 4). Furthermore, it binds specifically to MD-MBA-435, MD-MBA-231, and HUVEC and can be competed off by free VCN (Figure 5). Upon cell-

binding, A192-VCN displays remarkably different cytoplasmic staining patterns (Figure 6), which suggests that the fusion protein potentiates the internalization and loss of cell-surface integrin targets. Also, their intratumoral internalization can be saturated by excess treatment with unlabeled A192-VCN (Figure 9). Based on these observations, it may now be possible to engineer ELP disintegrin multimers that respond to clinical hyperthermia.[41] In addition, A192-VCN may now be explored as a biodegradable multimeric platform for the delivery of payloads, including radiological, chemotherapeutic, or protein-based agents.

CONCLUSIONS

This manuscript describes a unique disintegrin-polymer fusion that maintains specificity for the disintegrin's target in vitro and in vivo. Uptake occurs by a saturable process via specific attachment and internalization to heterodimeric integrin receptors located at the surface of both endothelial and cancer cells, as well as tumor neovasculature. With continued development, these fusion proteins may be useful carriers for therapeutic and imaging agents.

ASSOCIATED CONTENT

Supporting Information

Characterization of the integrin expression levels and VCN binding of HUVEC, MDA-MB-435, and MDA-MB-231 cells (Figure S1), as well as stability of A192-VCN multimers (Figure S2). This material is available free of charge via the Internet at http://pubs.acs.org.

AUTHOR INFORMATION

Corresponding Author

*E-mail: jamackay@usc.edu. Phone: 323-442-4118.

Author Contributions

†These authors contributed equally to this work (S.M.J. and J.A.G.).

Notes

The authors declare no competing financial interest.

ACKNOWLEDGMENTS

This work was made possible by the University of Southern California, the National Institute of Health R21EB012281 to J.A.M., and P30 CA014089 to the Norris Comprehensive Cancer Center, the USC Molecular Imaging Center, the USC Nanobiophysics Core Facility, the Translational Research Laboratory at the School of Pharmacy, the American Cancer Society IRG-58-007-48 and MSRG-12-034-01-CCE, the Stop Cancer Foundation, the USC Ming Hsieh Institute for Research on Engineering-Medicine for Cancer, the USC Wright Foundation, and the SC CTSI (NIH/NCRRlNCATS) through Grant UL1RR031986. S.M.J. is a recipient of a Malaysian Public Services Department scholarship. Thank you to J. Rohrs for editing the manuscript.

ABBREVIATIONS:

AmBaSar, 4-((8-amino-3,6,10,13,16,19-hexaazabicyclo [6.6.6] icosane-1-ylamino) methyl) benzoic acid; ELP, elastin-like polypeptide; DLS, dynamic light scattering; DOTA, 1,4,7,10-tetraazacyclododecane-1,4,7,10-tetraacetic acid; DTPA, diethylene triamine pentaacetic acid; R_h, hydrodynamic radius; SEC, size exclusion chromatography; PET, positron emission tomography; RDL, recursive directional ligation; T_t, transition temperature; VCN, vicrostatin

REFERENCES

(1) Sancey, L.; Garanger, E.; Foillard, S.; Schoehn, G.; Hurbin, A.; Albiges-Rizo, C.; Boturyn, D.; Souchier, C.; Grichine, A.; Dumy, P.; Coll, J. L. Clustering and internalization of integrin $\alpha_v\beta_3$ with a tetrameric RGD-synthetic peptide. *Mol. Ther.* **2009**, *17* (5), 837−43.

(2) Max, R.; Gerritsen, R. R. C. M.; Nooijen, P. T. G. A.; Goodman, S. L.; Sutter, A.; Keilholz, U.; Ruiter, D. J.; De Waal, R. M. W. Immunohistochemical analysis of integrin $\alpha_v\beta_3$ expression on tumor-associated vessels of human carcinomas. *Int. J. Cancer* **1997**, *71* (3), 320−324.

(3) Brooks, P. C.; Clark, R. A.; Cheresh, D. A. Requirement of vascular integrin $\alpha_v\beta_3$ for angiogenesis. *Science (New York, N.Y.)* **1994**, *264* (5158), 569−571.

(4) Albelda, S. M.; Mette, S. A.; Elder, D. E.; Stewart, R.; Damjanovich, L.; Herlyn, M.; Buck, C. A. Integrin distribution in malignant melanoma: Association of the β3 subunit with tumor progression. *Cancer Res.* **1990**, *50* (20), 6757−6764.

(5) Sengupta, S.; Chattopadhyay, N.; Mitra, A.; Ray, S.; Dasgupta, S.; Chatterjee, A. Role of $\alpha_v\beta_3$ integrin receptors in breast tumor. *J. Exp. Clin. Cancer Res.* **2001**, *20* (4), 585.

(6) Liapis, H.; Flath, A.; Kitazawa, S. Integrin $\alpha_v\beta_3$ expression by bone-residing breast cancer metastases. *Diagn. Mol. Pathol, Part B* **1996**, *5* (2), 127.

(7) Meerovitch, K.; Bergeron, F.; Leblond, L.; Grouix, B.; Poirier, C.; Bubenik, M.; Chan, L.; Gourdeau, H.; BOWLING, T.; Attardo, G. A novel RGD antagonist that targets both $\alpha_v\beta_3$ and $\alpha_5\beta_1$ induces apoptosis of angiogenic endothelial cells on type I collagen. *Vasc. Pharmacol.* **2003**, *40* (2), 77−89.

(8) Calvete, J. J.; Moreno-Murciano, M. P.; Theakston, R. D.; Kisiel, D. G.; Marcinkiewicz, C. Snake venom disintegrins: novel dimeric disintegrins and structural diversification by disulphide bond engineering. *Biochem. J.* **2003**, *372* (Pt 3), 725−34.

(9) Juárez, P.; Comas, I.; González-Candelas, F.; Calvete, J. J. Evolution of snake venom disintegrins by positive Darwinian selection. *Mol. Biol. Evol.* **2008**, *25* (11), 2391−2407.

(10) Reiss, S.; Sieber, M.; Oberle, V.; Wentzel, A.; Spangenberg, P.; Claus, R.; Kolmar, H.; Lösche, W. Inhibition of platelet aggregation by grafting RGD and KGD sequences on the structural scaffold of small disulfide-rich proteins. *Platelets* **2006**, *17* (3), 153−157.

(11) Pfaff, M.; McLane, M. A.; Beviglia, L.; Niewiarowski, S.; Timpl, R. Comparison of disintegrins with limited variation in the RGD loop in their binding to purified integrins $\alpha_{IIb}\beta_3$, $\alpha_v\beta_3$ and $\alpha_5\beta_1$ and in cell adhesion inhibition. *Cell Commun. Adhes.* **1994**, *2* (6), 491−501.

(12) Calvete, J. J.; Schaefer, W.; Soszka, T.; Lu, W.; Cook, J.; Jameson, B. A.; Niewiarowski, S. Identification of the disulfide bond pattern in albolabrin, an RGD-containing peptide from the venon of trimeresurus albolabris: Significance for the express of platelet aggregation inhibitory activity. *Biochemistry* **1991**, *30* (21), 5225−5229.

(13) Calvete, J. J.; Marcinkiewicz, C.; Monleón, D.; Esteve, V.; Celda, B.; Juárez, P.; Sanz, L. Snake venom disintegrins: evolution of structure and function. *Toxicon* **2005**, *45* (8), 1063−1074.

(14) Marcinkiewicz, C.; Vijay-Kumar, S.; McLane, M. A.; Niewiarowski, S. Significance of RGD loop and C-terminal domain of echistatin for recognition of $\alpha_{IIb}\beta_3$ and $\alpha_v\beta_3$ integrins and expression of ligand-induced binding site. *Blood* **1997**, *90* (4), 1565−1575.

(15) Fujii, Y.; Okuda, D.; Fujimoto, Z.; Horii, K.; Morita, T.; Mizuno, H. Crystal structure of trimestatin, a disintegrin containing a cell adhesion recognition motif RGD. *J. Mol. Biol.* **2003**, *332* (5), 1115−1122.

(16) Swenson, S.; Costa, F.; Minea, R.; Sherwin, R. P.; Ernst, W.; Fujii, G.; Yang, D.; Markland, F. S. Intravenous liposomal delivery of the snake venom disintegrin contortrostatin limits breast cancer progression. *Mol. Cancer Ther.* **2004**, *3* (4), 499−511.

(17) Minea, R.; Swenson, S.; Costa, F.; Chen, T. C.; Markland, F. S. Development of a novel recombinant disintegrin, contortrostatin, as an

effective anti-tumor and anti-angiogenic agent. *Pathophysiol. Haemostasis Thromb.* **2005**, *34* (4−5), 177−183.
(18) Minea, R. O.; Helchowski, C. M.; Zidovetzki, S. J.; Costa, F. K.; Swenson, S. D.; Markland, F. S., Jr. Vicrostatin − An anti-invasive multi-integrin targeting chimeric disintegrin with tumor anti-angiogenic and pro-apoptotic activities. *PLoS One* **2010**, *5* (6), e10929.
(19) Färber, K.; Synowitz, M.; Zahn, G.; Vossmeyer, D.; Stragies, R.; van Rooijen, N.; Kettenmann, H. An $\alpha_5\beta_1$ integrin inhibitor attenuates glioma growth. *Mol. Cell. Neurosci.* **2008**, *39* (4), 579−585.
(20) Kopeček, J.; Kopečková, P.; Minko, T.; Lu, Z.-R. HPMA copolymer−anticancer drug conjugates: design, activity, and mechanism of action. *Eur. J. Pharm. Biopharm.* **2000**, *50* (1), 61−81.
(21) Liu, W.; Dreher, M. R.; Furgeson, D. Y.; Peixoto, K. V.; Yuan, H.; Zalutsky, M. R.; Chilkoti, A. Tumor accumulation, degradation and pharmacokinetics of elastin-like polypeptides in nude mice. *J. Controlled Release* **2006**, *116* (2), 170−8.
(22) Behe, M.; Du, J.; Becker, W.; Behr, T.; Angerstein, C.; Márquez, M.; Hiltunen, J.; Nilsson, S.; Holmberg, A. Biodistribution, blood half-life, and receptor binding of a somatostatin-dextran conjugate. *Med. Oncol* **2001**, *18* (1), 59−64.
(23) Asai, D.; Xu, D.; Liu, W.; Garcia Quiroz, F.; Callahan, D. J.; Zalutsky, M. R.; Craig, S. L.; Chilkoti, A. Protein polymer hydrogels by in situ, rapid and reversible self-gelation. *Biomaterials* **2012**, *33* (21), 5451−5458.
(24) Hu, X.; Wang, X.; Rnjak, J.; Weiss, A. S.; Kaplan, D. L. Biomaterials derived from silk−tropoelastin protein systems. *Biomaterials* **2010**, *31* (32), 8121−8131.
(25) Kopeček, J. Hydrogel biomaterials: A smart future? *Biomaterials* **2007**, *28* (34), 5185−5192.
(26) Fujita, Y.; Mie, M.; Kobatake, E. Construction of nanoscale protein particle using temperature-sensitive elastin-like peptide and polyaspartic acid chain. *Biomaterials* **2009**, *30* (20), 3450−3457.
(27) Truong, M. Y.; Dutta, N. K.; Choudhury, N. R.; Kim, M.; Elvin, C. M.; Hill, A. J.; Thierry, B.; Vasilev, K. A pH-responsive interface derived from resilin-mimetic protein Rec1-resilin. *Biomaterials* **2010**, *31* (15), 4434−4446.
(28) Urry, D. W. Physical chemistry of biological free energy transduction as demonstrated by elastic protein-based polymers. *J. Phys. Chem. B* **1997**, *101* (51), 11007−11028.
(29) Urry, D. W. Free energy transduction in polypeptides and proteins based on inverse temperature transitions. *Prog. Biophys. Mol. Biol.* **1992**, *57* (1), 23−57.
(30) Shah, M.; Hsueh, P. Y.; Sun, G.; Chang, H. Y.; Janib, S. M.; MacKay, J. A. Biodegradation of elastin-like polypeptide nanoparticles. *Protein Sci.* **2012**, *21* (6), 743−50.
(31) McDaniel, J. R.; MacKay, J. A.; Quiroz, F. G. a.; Chilkoti, A. Recursive directional ligation by plasmid reconstruction allows rapid and seamless cloning of oligomeric genes. *Biomacromolecules* **2010**, *11* (4), 944−952.
(32) Golemis, E.; Adams, P. D. *Protein−Protein Interactions: A Molecular Cloning Manual*, 2nd ed.; Cold Spring Harbor Laboratory Press: Cold Spring Harbor, N.Y., 2005; p xiv, 938 p.
(33) Wu, Y.; Zhang, X.; Xiong, Z.; Cheng, Z.; Fisher, D. R.; Liu, S.; Gambhir, S. S.; Chen, X. microPET imaging of glioma integrin $\alpha_v\beta_3$ expression using ^{64}Cu-labeled tetrameric RGD peptide. *J. Nucl. Med.* **2005**, *46* (10), 1707−1718.
(34) Cai, H.; Fissekis, J.; Conti, P. S. Synthesis of a novel bifunctional chelator AmBaSar based on sarcophagine for peptide conjugation and 64Cu radiolabelling. *Dalton Trans.* **2009**, *27*, 5395−5400.
(35) Janib, S. M.; Pastuszka, M.; Aluri, S.; Folchman-Wagner, Z.; Hsueh, P. Y.; Shi, P.; Yi, A.; Cui, H.; Mackay, J. A. A quantitative recipe for engineering protein polymer nanoparticles. *Polym. Chem.* **2014**, *5* (5), 1614−1625.
(36) Janib, S. M.; Liu, S.; Park, R.; Pastuszka, M. K.; Shi, P.; Moses, A. S.; Orosco, M. M.; Lin, Y. A.; Cui, H.; Conti, P. S.; Li, Z.; MacKay, J. A. Kinetic quantification of protein polymer nanoparticles using noninvasive imaging. *Integr. Biol. (Cambridge, U.K.)* **2013**, *5* (1), 183−94.
(37) Cai, W.; Zhang, X.; Wu, Y.; Chen, X. A thiol-reactive ^{18}F-labeling agent, *N*-[2-(4−18F-fluorobenzamido)ethyl]maleimide, and synthesis of RGD peptide-based tracer for PET imaging of $\alpha_v\beta_3$ integrin expression. *J. Nucl. Med.* **2006**, *47* (7), 1172−1180.
(38) Sawant, R.; Torchilin, V. Challenges in development of targeted liposomal therapeutics. *AAPS J.* **2012**, *14* (2), 303−315.
(39) Torchilin, V. P. Micellar nanocarriers: Pharmaceutical perspectives. *Pharm. Res.* **2007**, *24* (1), 1−16.
(40) Heneweer, C.; Holland, J. P.; Divilov, V.; Carlin, S.; Lewis, J. S. Magnitude of enhanced permeability and retention effect in tumors with different phenotypes: ^{89}Zr-albumin as a model system. *J. Nucl. Med.* **2011**, *52* (4), 625−633.
(41) MacKay, J. A.; Chilkoti, A. Temperature sensitive peptides: Engineering hyperthermia-directed therapeutics. *Int. J. Hyperthermia.* **2008**, *24* (6), 483−495.
(42) Pace, C. N.; Vajdos, F.; Fee, L.; Grimsley, G.; Gray, T. How to measure and predict the molar absorption coefficient of a protein. *Protein Sci.* **1995**, *4* (11), 2411−2423.
(43) Meyer, D. E.; Chilkoti, A. Quantification of the effects of chain length and concentration on the thermal behavior of elastin-like polypeptides. *Biomacromolecules* **2004**, *5* (3), 846−851.